Stochasticity of the magnon parametron

Mehrdad Elyasi,[1] Eiji Saitoh,[1,2,3,4,5] and Gerrit E. W. Bauer[1,2,3,6]

[1]*Institute for Materials Research, Tohoku University, Sendai 980-8577, Japan*
[2]*WPI Advanced Institute for Materials Research, Tohoku University, Sendai 980-8577, Japan*
[3]*Center for Spintronics Research Network, Tohoku University, Sendai 980-8577, Japan*
[4]*Department of Applied Physics, University of Tokyo, Hongo, Tokyo 113-8656, Japan*
[5]*Advanced Science Research Center, Japan Atomic Energy Agency, Tokai 319-1195, Japan*
[6]*Zernike Institute for Advanced Materials, University of Groningen, 9747 AG Groningen, Netherlands*

(Received 23 September 2021; revised 3 January 2022; accepted 7 January 2022; published 3 February 2022)

Unconventional computing schemes based on bistable systems ("Ising spins") may supersede conventional computing paradigms. The "magnon parametron" is an Ising spin that forms as a result of parametric excitation of a ferromagnetic particle by microwaves beyond a certain threshold. This Ising spin becomes unstable at a second threshold power at which a high-frequency telegraph noise emerges. We explain the experimentally observed stochastic switching ("p-bit" characteristics) at room temperature by the Suhl instability of the uniform magnetization precession.

DOI: 10.1103/PhysRevB.105.054403

I. INTRODUCTION

An Ising spin is a magnetic moment with a large uniaxial anisotropy that reduces the quantum degree of freedom of the Heisenberg spin on the Bloch sphere to just 2, i.e., up and down. Naturally, any bistable system with a phase space of two distinct and stable configurations may be called a pseudo-Ising spin, such as a fixed ferromagnetic needle in which the magnetization can point only into the two directions that minimize the free energy. An Ising spin with noise-activated transitions can operate as a probabilistic bit (p-bit), which in its steady state is a statistical mixture of the two levels. Ising spins are not useful as qubits because the large energy barrier prevents spin rotations on the Bloch sphere, but an ensemble of them can form a platform for unconventional computing algorithms. Switchable, but thermally stable, Ising spins are elements of "Ising machines" that can solve hard optimization problems [1–5], while networks of p-bits can factorize large integers [6]. A large number (∼2000) of highly connected pseudo-Ising spins formed by optical parametric oscillators operate by phase measurements with feedback [2–4]. However, optical implementations have a large footprint and are not scalable. Quantum coherent networks can perform additional tasks such as quantum annealing, adiabatic evolution, or gated quantum operations [7–12], but are even more difficult to realize. Here we explain the underlying physics of a recent implementation of an Ising spin system, viz., the "magnon parametron" [13], a promising device for alternative computing schemes.

Parametric pumping is a standard method to excite large oscillations in a harmonic oscillator by a phase-matched drive at twice its resonance frequency ω_0. The minimum model is the Hamiltonian $\mathcal{H} = \hbar\omega_0 a^\dagger a$, where $a^\dagger(a)$ creates (annihilates) a boson, augmented by a nonlinear interaction with the classical photon field $H = Pe^{2i\omega_0 t}a^\dagger a^\dagger + \text{H.c.}$ When the amplitude P exceeds a certain threshold the system becomes unstable. The steady state $\langle a\rangle$ has an amplitude limited by dissipation and spontaneously acquires one of the energetically equivalent phases of $\phi_P/2 + 0$ or $\phi_P\ /2 + \pi$, where $\phi_P = \arg P$ and $2\text{mod}[\arg\langle a\rangle, 2\pi] = \text{mod}[\phi_p, 2\pi]$. Makiuchi *et al.* [13] demonstrated Ising spin characteristics in a parametrically pumped magnetic disk that above a second threshold showed the controlled stochastic switching that qualifies it as a p-bit. The underlying mechanism of this stochasticity has not yet been explained, however. Magnons are set apart from, e.g., phonons [14,15] by their highly tunable, anisotropic and nonmonotonic dispersions, leading to phenomena such as Bose-Einstein condensation and deterministic quantum entanglement [16–20]. In this article, by analytic and numerical calculations, we provide a microscopic picture of the observed stochasticity in terms of the Suhl instability [16,21–23], i.e., the decay of the uniform (Kittel) magnon into a pair of degenerate "wing" magnons with opposite momenta $\pm k \neq 0$.

II. MODEL

Figure 1(a) sketches a thin ferromagnetic disk of thickness d and radius r, uniformly magnetized along the in-plane magnetic field $\vec{H}_{\text{ext}} \| \hat{z}$. For parametric pumping, the microwave magnetic field $\vec{h}_{\text{mw}}$ of a cavity or a coplanar waveguide mode with frequency ω_p is also parallel to the magnetization. Figure 1(b) shows the magnon frequency dispersions $\omega_{\vec{k}}$ of the lowest magnon subband of a $d = 50$-nm-thick film for in-plane wave vectors $\theta_{\vec{k}} = 0$ ($\vec{k} \| \hat{z}$) and $\theta_{\vec{k}} = \pi/2$ ($\vec{k} \perp \hat{z}$) and a constant as a function of position along $\hat{x}$ [24–26], using well-established parameters for yttrium iron garnet (YIG) with the gyromagnetic ratio $\gamma = 28$ GHz/T and the spin

 ©2022 American Physical Society

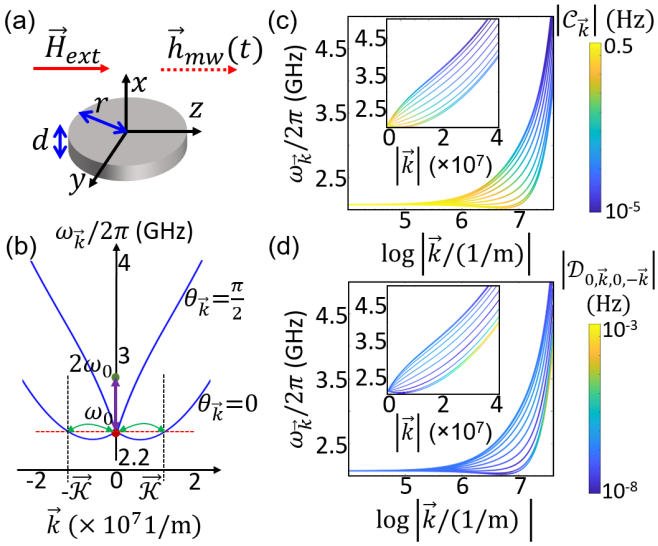

FIG. 1. Model. (a) A magnetic disk of thickness d and radius r under static and microwave magnetic fields. (b) The dispersion envelope of magnons in a film with constant magnetization along $\hat{x}$ for $d = 50$ nm and $H_{\mathrm{ext}} = 35$ mT. The green arrows indicate four-magnon scattering processes involving the Kittel mode. The purple line indicates parametric pumping of the Kittel mode. (c) The parametric excitation coefficient $\mathcal{C}_{\vec{k}}$ of the magnon pairs overlaid on the dispersion for several values of $\theta_{\vec{k}}$ from 0 to $\pi/2$, only for the modes that are nodeless along the thickness. (d) Similar to panel (c) but for the four-magnon scattering coefficient $\mathcal{D}_{0,\vec{k},0,-\vec{k}}$. The insets of panels (c) and (d) plot the data of the main panels on a linear momentum scale.

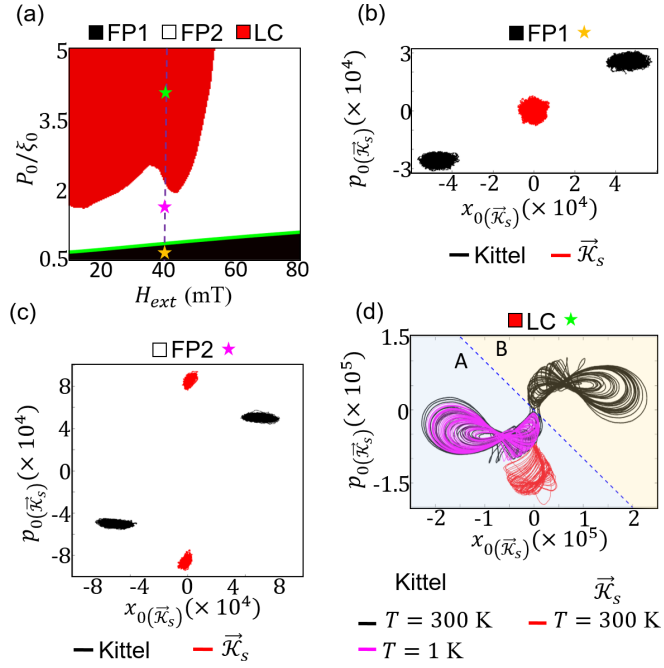

FIG. 2. Calculated steady-state dynamics of a magnet in a microwave cavity. (a) The dependence of the steady-state class on the Kittel mode amplitude P_0 driven by the mircrowaves and the dc magnetic field H_{ext}. (b)–(d) Examples for the three distinct classes, corresponding to the stars of the same color in panel (a), $P_0/\xi_0 = 0.7$, 1.7, and 3.8, respectively, while $H_{\mathrm{ext}} = 40$ mT. (b) FP1: Fixed point, the Kittel mode parametrically driven beyond threshold, while the $\vec{\mathcal{K}}_s$ standing wave is at vacuum. (c) FP2: Fixed point, the Kittel mode and the $\vec{\mathcal{K}}_s$ standing wave parametrically and Suhl instability driven, respectively. In panels (b) and (c), $T = 3 \times 10^5$ K for clarity. (d) LC: Limit cycle to chaos. A case with large transition rate from one attractor region of the Kittel mode to the other, at $T = 300$ K, and no transition for $T = 1$ K is also shown. The two attractor regions A and B are indicated.

stiffness $D = 5.5 \times 10^{-17}\mathrm{Tm}^2$ [27]. ω_0 is the frequency of the Kittel mode, and higher subbands are not shown since $\omega_{\vec{k}_{\mathrm{dip}}} + 4\gamma D/d^2 > \omega_0$, where the frequency minimum $\omega_{\vec{k}_{\mathrm{dip}}}$ is caused by the magnetodipolar interaction. The two valleys in the magnon dispersion are instrumental for the Suhl instability and (for $d = 50$ nm) exist when $r \gtrsim 0.5$ μm. Here we adopt $r = 50$ μm, large enough to adopt a continuous dispersion for the $\theta_{\vec{k}} = 0$ modes degenerate with the Kittel mode (see below).

$\vec{h}_{\mathrm{mw}}(t)$ of the photon with frequency $\omega_p = 2\omega_0$ parametrically interacts with the Kittel mode and the degenerate magnon pairs, $\gamma|h_{\mathrm{mw}}|\mathcal{C}_{\vec{k}}(c^\dagger_{-\vec{k}}c^\dagger_{\vec{k}} + \mathrm{H.c.})$, where $c_{\vec{k}}$ annihilates the $\vec{k}$ magnon mode, and $\mathcal{C}_{\vec{k}}$ is the coefficient plotted in Fig. 1(c). With increasing $|h_{\mathrm{mw}}|$ the mode with the largest $\mathcal{C}_{\vec{k}}$ becomes unstable at a critical value of $\gamma|h_{\mathrm{mw}}|\mathcal{C}_{\vec{k}} = \xi_{\vec{k}}/2$, where $\xi_{\vec{k}} \approx \alpha_{\mathrm{G}}\omega_{\vec{k}}$ is the magnon dissipation rate in terms of α_{G}, the Gilbert damping constant. $|\mathcal{C}_{\vec{k}}|$ is maximal for small wave vectors [see Fig. 1(c)], which implies that the Kittel mode becomes unstable first. The parametrically driven Kittel mode excites other magnons via the four-magnon scattering term $c_0^\dagger c_0^\dagger c_{\vec{k}} c_{-\vec{k}} + \mathrm{H.c.}$, with the corresponding coefficients $\mathcal{D}_{0,\vec{k},0,-\vec{k}}$ [see Fig. 1(d)]. This is the threshold process introduced first by Suhl [21]. The instability happens first for the degenerate modes with the largest $|\mathcal{D}_{0,\vec{k},0,-\vec{k}}|$, i.e., for $\theta_{\vec{k}} = 0$ and large $|\vec{k}|$, and thereby limits the effective system to three modes, the parametrically pumped Kittel mode and a pair of magnons with large wave vectors, $\pm\vec{\mathcal{K}}$. In the rotating frame of $\omega_p/2$, our Hamiltonians [16,28,29] are

$$H = \sum_{\vec{k}\in\{0,\pm\vec{\mathcal{K}}\}} \Delta\omega_{\vec{k}} c^\dagger_{\vec{k}} c_{\vec{k}} + H_{m,\mathrm{NL}} + P_0(c_0^\dagger c_0^\dagger + \mathrm{H.c.}),$$

$$H_{m,\mathrm{NL}} = \sum_{\vec{k}\in\{0,\pm\vec{\mathcal{K}}\}} \Big[\mathcal{D}_{\vec{k},\vec{k},\vec{k},\vec{k}} c^\dagger_{\vec{k}} c_{\vec{k}} c^\dagger_{\vec{k}} c_{\vec{k}} + \sum_{\vec{k}'\in\{0,\pm\vec{\mathcal{K}}\}} (1-\delta_{\vec{k},\vec{k}'}) \mathcal{D}_{\vec{k},\vec{k},\vec{k}',\vec{k}'} c^\dagger_{\vec{k}} c_{\vec{k}} c^\dagger_{\vec{k}'} c_{\vec{k}'} \Big] + [\mathcal{D}_{0,-\vec{\mathcal{K}},0,\vec{\mathcal{K}}} c_0^\dagger c_0^\dagger c_{-\vec{\mathcal{K}}} c_{\vec{\mathcal{K}}} + \mathrm{H.c.}], \quad (1)$$

where $\Delta\omega_{\vec{k}} = \omega_{\vec{k}} - \omega_p/2$ and $P_0 = \gamma|h_{\mathrm{mw}}|\mathcal{C}_0$. The dipolar and exchange interactions and (if present) the magnetic anisotropy all contribute to the four-magnon scattering coefficients $\mathcal{D}$ and the two-magnon–one-photon coupling with coefficient $\mathcal{C}_{\vec{k}}$. We compute the numbers in Figs. 2(c), 2(d), and 8(a) from complex but well-known expressions of these coefficients for thin films [28,29].

Theoretical approaches to the magnetization dynamics usually start from the stochastic Landau-Lifshitz-Gilbert equation that even with a quantum mechanical thermostat [30] is not suited to address the physics of the emerging quantum magnonics. Typical quantum effects emerge in the correlations between two distinct orthonormal magnon modes. These can be captured only by a model that tracks the dynamics of individual and interacting modes. While we address here the classical dynamics at room temperature, our method is well suited to calculate quantum correlations [16] that appear when the temperature is lowered [31]. We, therefore, start from the (Lindblad) equation of motion of the density matrix ρ with elements $\rho_{i,j} = |i\rangle\langle j|$, where $|i(j)\rangle$ is a many-body number (Fock) state of the magnon system, that reads

$$\dot{\rho} = -i[H, \rho] + L_d, \tag{2}$$

where L_d is the dissipation operator of the magnons in contact with a thermal bath at temperature T [see Appendix A]. We can solve this equation exactly only for small magnets [16,32], but solve here a time-dependent Langevin equation with approximations that are valid under the experimental conditions [13,33]. Without drive, ρ describes a magnon gas at thermal equilibrium with the bath. Here we use a rather large damping parameter $\xi_0 = 5$ MHz corresponding to $\alpha_G \sim 2 \times 10^{-3}$ for computational convenience. A larger damping parameter ξ_0 accelerates numerical convergence to the steady state. The relevant parameter that governs the dynamics is P_0/ξ_0, which does not change for a large range of ξ_0.

III. STEADY-STATE CLASSES

We first classify the steady-state dynamics in terms of a "phase diagram" of our three-mode system by inspection of the long-time solutions of the stochastic differential (Langevin) equation of motion, derived from the Lindblad equation (2) by disregarding the third-order derivatives of the Wigner distribution function, as described in Appendix A [34,35]. This approach captures Gaussian fluctuations, i.e., up to the second moment and is valid when sufficiently damped ($\mathcal{D} \ll \xi_0$) and the steady state is not chaotic. It is basically equivalent to the stochastic Landau-Lifshitz-Gilbert equation to leading order in the nonlinearities, but uniquely allows the tracking of individual magnon modes in the presence of interactions.

We assume microwaves tuned to $\Delta\omega_0 = 0$ that drive the Kittel mode to an amplitude P_0. The other control parameter is the applied static magnetic field $H_{\rm ext}$. The smallest positive solution for $x = |\alpha_0|^2$, where $\alpha_0 = \langle c_0 \rangle$ is the mean field of the Kittel mode, governs $\theta_{\vec{\mathcal{K}}}$ and $\vec{\mathcal{K}}$ of the magnon pair that reaches the Suhl instability first:

$$\left(\mathcal{D}^2_{0,\vec{\mathcal{K}},0,-\vec{\mathcal{K}}} - \mathcal{D}^2_{0,0,\vec{\mathcal{K}},\vec{\mathcal{K}}}\right)x^2 - 2\Delta_{\vec{\mathcal{K}}}\mathcal{D}_{0,0,\vec{\mathcal{K}},\vec{\mathcal{K}}}x - \xi^2_{\vec{\mathcal{K}}}/4 - \Delta^2_{\vec{\mathcal{K}}} = 0. \tag{3}$$

Below the Suhl instability but above the parametric instability threshold, $|\alpha_0|^2 = \sqrt{P_0^2 - \xi_0^2/4}/2|\mathcal{D}_{0,0,0,0}|$. By minimizing Eq. (3) with respect to $\theta_{\vec{k}}$ and $|\vec{k}|$, we find that the $\pm\vec{\mathcal{K}}$ magnon pair lies in the $\theta_{\vec{k}} = 0$ band. We may combine the $\pm\vec{\mathcal{K}}$ pair of propagating waves as $c_{\pm\vec{\mathcal{K}}} = c_{\vec{\mathcal{K}}_s} e^{\mp iq/2}$ [36–38], where the phase q is a free phase that governs the position of the standing wave nodes and $\vec{\mathcal{K}}_s$ is its mode index.

Figure 2(a) shows the steady-state classes as a function of $H_{\rm ext}$ and P_0 at $T = 0$ K. The green line in Fig. 2(a) is an analytic solution of Eq. (3) using the four-magnon scattering parameters of the unstable mode at each $H_{\rm ext}$ [see Fig. 8(a), Appendix D]. Figures 2(b)–2(d) illustrate the phase-space dynamics of each class for a fixed magnetic field. Figures 2(b) and 2(c) show the trajectories in the time interval $t = 50$–80 μs, starting from 100 random initial values of $\phi_{0(\vec{\mathcal{K}}_s)}$ in $c_{0(\vec{\mathcal{K}}_s)} = e^{i\phi_{0(\vec{\mathcal{K}}_s)}}$ at $t = 0$. Here we chose a high temperature, $T = 3 \times 10^5$ K, to emphasize the dynamic stability. The trajectories are the time-dependent $x_{0(\pm\vec{\mathcal{K}})} = (c_{0(\vec{\mathcal{K}}_s)} + c^\dagger_{0(\vec{\mathcal{K}}_s)})/2$ and $p_{0(\vec{\mathcal{K}}_s)} = -i(c_{0(\vec{\mathcal{K}}_s)} - c^\dagger_{0(\vec{\mathcal{K}}_s)})/2$ in phase space. The position x_0 and the momentum p_0 of the harmonic oscillator that represents the Kittel mode correspond to the amplitudes of the dynamic magnetization, m_x and m_y. We picture the steady states of the excited system in the rotating frame of the Kittel mode frequency. The two uniform precessional modes of the magnetization are then mapped on two fixed points in (x_0, p_0) phase space with equal modulus and phase difference of π. The distinct classes of the Kittel mode are the fixed points FP1 and FP2. For a given $H_{\rm ext}$ and small $P_0 > \xi_0/2$ (FP1), it has two equivalent stable fixed points, viz., the Ising spin up and down states, while the standing wave mode fluctuates around the origin [see Fig. 2(b)]. When P_0 satisfies Eq. (3), the Suhl instability drives the $\pm\vec{\mathcal{K}}$ pair, leading to the FP2 steady state in which the Kittel fixed points persist, and $\vec{\mathcal{K}}_s$ settles into a fixed point at a distance from the origin with a phase spontaneously chosen out of two mirror symmetric values [see Fig. 2(c)]. A third distinct class is the limit cycle (LC) illustrated in Fig. 2(d), now at realistic temperatures. Here the Kittel mode follows large amplitude trajectories in mirror symmetric regions of phase space (see also Appendix D). With increasing P_0, the paths cross the boundaries between the attractor regions A and B, i.e., the Ising spin flips. The thermal activation is evident in Fig. 2(d) in which we compare switching at high $T = 300$ K (black curve) and low $T = 1$ K (purple curve) by way of single representative trajectories in the interval $t = 20$–320 μs. In Appendix D, we discuss the dependence of the limit cycle trajectories on P_0 (see Fig. 7 and Appendix D) and analytically explain the origin of FP2 to LC transition and its dependence on $H_{\rm ext}$ (see Fig. 8 and Appendix D).

Four-magnon scatterings are responsible for auto-oscillation (limit cycle) steady states that with increasing excitation power bifurcate and lead to chaotic dynamics [22]. Here we demonstrate that limit cycle dynamics of the magnon parametrons lead to stochastic switching between two otherwise isolated regions in phase space. The enhancement of stochastic switching is unique; it has, for instance, not been reported in photonic parametrons without analogous four boson interactions.

For a fixed-input amplitude P_0, an array of these magnets in the stable Ising spin operation can operate as a coherent Ising machine. In the following, we assess the potential of the device as p-bit by a quantitative treatment of the stochasticity.

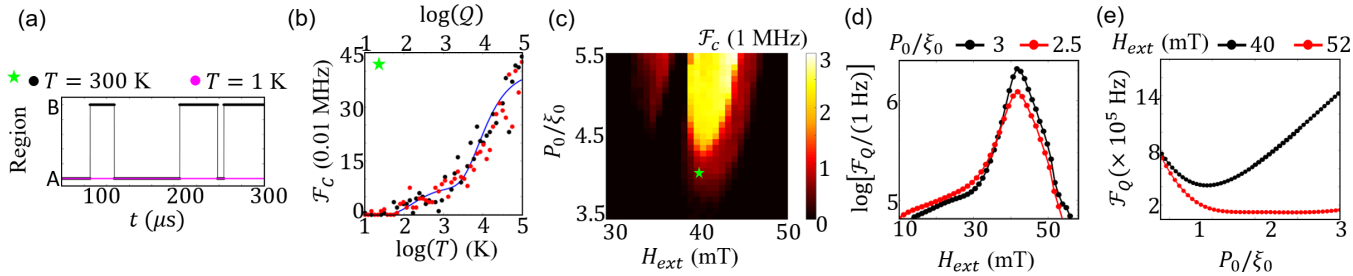

FIG. 3. Stochasticity. Panels (a)–(c) were obtained from classical calculations, while panels (d) and (e) were obtained from quantum calculations. (a) The region of the Kittel mode state shown in Fig. 2(d) for $T = 1$ K and $T = 300$ K. (b) The dependence of the transition frequency $\mathcal{F}_C$ on T (black dots) and $\mathcal{Q}$ (red dots), for $H_{\rm ext} = 40$ mT and $P_0/\xi_0 = 3.85$, as in panel (a) and Fig. 2(d). (c) $\mathcal{F}_C$ as a function of $H_{\rm ext}$ and P_0/ξ_0, at $T = 3 \times 10^5$ K. The green star is the same $(P_0, H_{\rm ext})$ point as in the phase diagram plotted in Figs. 2(a) and 2(d). (d) The dependence of the tunneling frequency $\mathcal{F}_Q$ on $H_{\rm ext}$ for two values of $P_0/\xi_0 = 2.5$ and 3. (e) The dependence of $\mathcal{F}_Q$ on P_0/ξ_0 for $H_{\rm ext} = 40$ and 52 mT, respectively. The scaling coefficient $\mathcal{Q} = 5 \times 10^9$ in panels (d) and (e), and $T = 0$ K.

IV. STOCHASTICITY

Below the Suhl instability threshold, the Ising spin is remarkably stable. The lower bound for the transition time τ between the two stable fixed points (derived in Appendix C 2) is

$$\ln\tau \gtrsim \ln[\pi(1+2n_{\rm th})\sqrt{(1+2\mathcal{R})/2\mathcal{R}^2}/2\xi_0] + [(1+2\mathcal{R})\ln(1+2\mathcal{R}) - 2\mathcal{R}]|K_0|(1+2n_{\rm th})/2, \quad (4)$$

where $\mathcal{R} = \sqrt{\mu^2-1}/2 + 1 - |K_0|(1+2n_{\rm th}) - 1$, $\mu = 2P_0/\xi_0$, and $K_0 = 2\mathcal{D}_{0,0,0,0}/\xi_0$. Above the parametric instability threshold but below the Suhl instability ($\mu = 1.1$) for typical values of $|\mathcal{D}_{0,0,0,0}| = 1.5 \times 10^{-4}$ Hz [see Fig. 8(a)], $\omega_0/2\pi = 2.5$ GHz [see Fig. 1(b)], and $T = 300$ K, this number becomes astronomically large, $\tau \gg \exp(1.4 \times 10^4)$ s. In the absence of four-magnon scatterings, the Kittel mode hopping time in Eq. (4) monotonically increases with increasing excitation power P_0 or μ. Therefore, the observation made by Makiuchi *et al.* [13] that, beyond a second threshold above the parametric instability, the hopping rate becomes large (hopping time becomes small) cannot be explained by a macrospin. As shown in the following, driving the system into a LC of the Kittel plus $\pm\vec{\mathcal{K}}$ modes by a sufficiently large μ enormously enhances the switching rate [see Fig. 2(d)]. We, therefore, conclude that the parametrically driven Suhl instability and the LC dynamical phase explain the observation of stochastic switching at the experimental power levels and room temperature.

The telegraph noise of the Kittel mode at $T = 300$ K in Fig. 3(a) reflects the thermally activated crossover trajectories in Fig. 2(d). The calculated number of switches N_t within $t_e = 100$ μs, averaged for several random initial conditions, leads to the transition frequencies $\mathcal{F}_C = N_t/t_e$ plotted in Fig. 3(b) as a function of T (black dots). The form $l_1 e^{-\lambda_1/T} + l_2 e^{-\lambda_2/T}$, with attempt frequencies $l_1 = 32 \times 10^4$ Hz and $l_2 = 8.1 \times 10^4$ Hz and energy well depths $\lambda_1 = 7.98 \times 10^3 \times k_B/2\pi\hbar$ GHz and $\lambda_2 = 1.5 \times 10^2 \times k_B/2\pi\hbar$ GHz fits the calculations well (blue curve). We also compute the $\mathcal{Q}$ dependence of the transition frequency at $T = 1$ K, where $\mathcal{Q}$ is the scaling factor of the four-magnon scattering coefficient $\mathcal{QD}$ that is inversely proportional to the volume of the magnet V_m. The increased interaction reduces the magnon amplitudes while preserving the topology in phase space. The red dots in Fig. 3(b) show enhanced switching rates for either increasing temperature or decreasing volume. Figure 3(c) shows the dependence of $\mathcal{F}_C$ on $H_{\rm ext}$ and P_0 at $T = 3 \times 10^5$ K. Makiuchi *et al.* [13] observed switching frequencies of ∼0.01–0.1 Hz at room temperature, depending on the power beyond a second threshold. As explained above, this is not possible without the Suhl instability. The experimental sample is too large for direct modeling, and the approximation of a constant magnetization over the film thickness breaks down in thicker samples in which higher perpendicular standing spin waves play a role. Nevertheless, we can still draw conclusions from the identical scaling of T and $\mathcal{Q}$ in Fig. 3(b). The experimental sample volume is ∼30 times larger than the sample considered here. Since $\mathcal{Q} \propto 1/V_m$, our model applies to the experiments for $\mathcal{Q} = 1/30$. By repeating the calculations for a scaling factor of $\mathcal{Q} = 1/30$, we effectively address a magnet that is 30 times larger than that for $\mathcal{Q} = 1$. The result of $\mathcal{F}_C \sim 0.01$ Hz at $T = 300$ K agrees with the lower end of the experimental observations. The predicted strong and nonmonotonic dependence of $\mathcal{F}_C$ on $H_{\rm ext}$ in Fig. 3(c) also agrees with experimental findings. The substantial enhancement of the stochasticity is due to the large-amplitude LC dynamics near the saddle node at the origin. Since a limit cycle broadens the distribution function when compared to a fixed point, the thermally activated switching through the saddle node becomes more efficient. At a fixed $H_{\rm ext}$, increasing P_0 leads to increasing LC oscillation amplitude and doublings (see Fig. 7 and Appendix D) and, therefore, to an increase in $\mathcal{F}$. At fixed P_0 the amplitude of the LC oscillations depends on $H_{\rm ext}$ via $\mathcal{D}$ [see Fig. 8(a)], with a maximum at $H_{\rm ext} \sim 40$ mT [see Appendix D and Fig. 8(d)] of $\mathcal{F}_C$ [see Fig. 3(c)]. From the dependence of $\mathcal{F}$ on $\mathcal{Q} \propto 1/V_m$ [see Fig. 3(b)] follows that reducing the sample to a dot with a 1-μm radius enhances the hopping rate by 7–8 orders of magnitude to ∼MHz.

The field of magnonics is moving to identify quantum effects [39] by extending experiments to smaller systems and low temperatures. Smaller samples correspond to larger nonlinear coefficients [large $\mathcal{Q}$, see Fig. 3(b)] and at low temperature quantum fluctuations are enhanced, which means

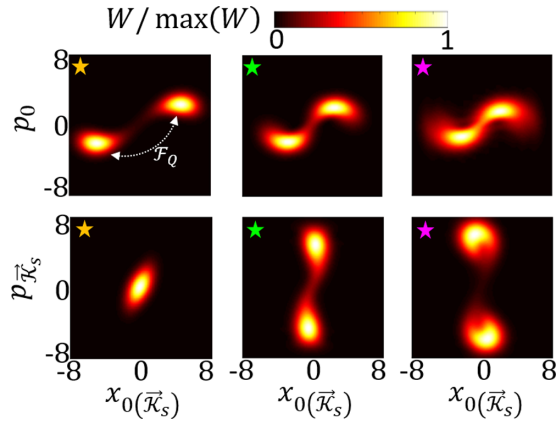

FIG. 4. Quantum steady states. The top (bottom) panels are the Wigner function of the Kittel mode ($\mathcal{K}$ standing wave) normalized by the maximum value. The left, middle, and right panels correspond to the star of the same color as in Fig. 2(a) as well as Figs. 2(b)–2(d) of the main text, i.e., in the FP1 (stable Ising), FP2, and stochastic (LC) regions, respectively. The scaling of four-magnon scattering coefficients $\mathcal{Q} = 5 \times 10^8$, 2×10^9, and 4×10^9 is shown in the panels from left to right, respectively.

that the approximation used to derive the Langevin evolution breaks down. In order to gauge the limitations of our method, we return to the original Lindblad equation and solve it numerically exact in number (Fock) space to reliably treat the quantum, classical, and crossover regimes. In order to quantify the stochasticity from the exact solution, $\mathcal{F}_Q$, we calculate up to 20 smallest amplitude eigenvalues $\mathcal{E}$ of the right-hand side of Eq. (2). $\mathcal{E} = 0$ corresponds to the ground-state density matrix [see Fig. 4 and Appendix B]. The first two eigenvalues with smallest but nonzero $|\mathrm{Re}\mathcal{E}|$ while $\mathrm{Im}\mathcal{E} = 0$ determine the tunneling frequencies (see Appendix C 1). One of these eigenvalues corresponds to the tunneling frequency of the Kittel mode, $\mathcal{F}_Q$ [40] [see top left panel of Fig. 6(a)], as explained in Appendix C 1. The other corresponds to the tunneling frequency of the $\vec{\mathcal{K}}_s$ mode. Below the parametric and Suhl instability thresholds, such an eigenvalue does not exist for either of the modes and the $\vec{\mathcal{K}}_s$ mode, respectively. The choice of $\mathcal{Q} = 5 \times 10^9$ allows us to limit the Hilbert space to ∼1000, which is our computational limit. Figure 3(d) shows $\mathcal{F}_Q$ as a function of H_{ext} for two values of $P_0/\xi_0 = 2.5$ and 3 that crosses both the LC and FP2 regions [see Fig. 2(a)]. $\mathcal{F}_Q$ is peaked at $H_{\mathrm{ext}} \sim 40$ mT, similar to that of $\mathcal{F}_C$ in Fig. 3(c), and decreases sharply for H_{ext} in the FP2 region. Figure 3(d) shows that $\mathcal{F}_Q$ decreases monotonically with increasing P_0 for $H_{\mathrm{ext}} = 52$ mT where the classical steady state does not enter the LC region. However, for $H_{\mathrm{ext}} = 40$ mT, where the steady state changes from FP1 to FP2 and then becomes LC, by increasing P_0, $\mathcal{F}_Q$ first decreases and then increases substantially. Based on the fit in Fig. 3(b), for $\mathcal{Q} = 10^9$, $\mathcal{F}_C \sim 1$ MHz, which is in the same range as expected from $\mathcal{F}_Q$ in Figs. 3(d) and 3(e). Therefore, the Langevin approach should be valid to describe parametrically and resonantly driven ferromagnets including a quantitative description of magnon quantum correlations such as entanglement [16,31].

V. CONCLUSION

We study the bistable Ising spin system emulated by a ferromagnetic disk parametrically excited in a microwave cavity as a function of temperature, magnetic field, and excitation power. The Suhl decay of the Kittel mode into a degenerate pair of magnons with large wave vectors drastically enhances the random switching between pseudospin states, explaining the recent experimental observation [13]. The discovered stochasticity principle requires degeneracy of the parametrically excited boson and nonlinear four-boson interactions among the degenerate modes. The in-plane magnetized thin films is a unique natural system that satisfies the latter conditions. While the predicted phenomena are unique to magnetic materials, results may be extrapolated to metamaterials and quantum optics, in which parametrons are frequently modeled as Ising spins. We conclude that parametrically excited magnetic particles are attractive building blocks for coherent Ising machines, as well as stochastic information applications. Our methods are also well suited to predict and describe the quantum effects anticipated in the next generation of experimental magnonics.

ACKNOWLEDGMENTS

We acknowledge support by JSPS KAKENHI (Grants No. 19H00645 and No. 21K13847), and JST CREST (Grant No. JPMJCR20C1).

APPENDIX A: EQUATIONS OF MOTION

In this section, we derive the Langevin equation of motion. The starting point is the (Lindblad) equation of motion (EOM) of the density matrix ρ,

$$\dot{\rho} = -i[H, \rho] + L_d, \tag{A1}$$

where H' is the Hamiltonian for the interacting magnons in which the Kittel mode is driven by P_0,

$$\begin{aligned} H &= H_{m,L} + H_{m,\mathrm{NL}} + (P_0 c_0^\dagger c_0^\dagger + \mathrm{H.c.}), \\ H_{m,L} &= \sum_{\vec{k}\in 0,\pm\mathcal{K}} \Delta\omega_{\vec{k}} c_{\vec{k}}^\dagger c_{\vec{k}} \\ H_{m,\mathrm{NL}} &= \sum_{\vec{k}\in 0,\pm\mathcal{K}} \Bigg[\mathcal{D}_{\vec{k},\vec{k},\vec{k},\vec{k}} c_{\vec{k}}^\dagger c_{\vec{k}} c_{\vec{k}}^\dagger c_{\vec{k}} \\ &\quad + \sum_{\vec{k}'\in 0,\pm\mathcal{K}} (1-\delta_{\vec{k},\vec{k}'}) \frac{1}{2} \mathcal{D}_{\vec{k},\vec{k},\vec{k}',\vec{k}'} c_{\vec{k}}^\dagger c_{\vec{k}} c_{\vec{k}'}^\dagger c_{\vec{k}'} \Bigg] \\ &\quad + [\mathcal{D}_{0,-\mathcal{K},0,\mathcal{K}} c_0^\dagger c_0^\dagger c_{-\mathcal{K}} c_{\mathcal{K}} + \mathrm{H.c.}], \end{aligned} \tag{A2}$$

and

$$\begin{aligned} L_d = \sum_{\vec{k}\in\{0,\pm\mathcal{K}\}} \xi_{\vec{k}} \big[& n_{\mathrm{th}}(\omega_{\vec{k}}) (c_{\vec{k}} \rho c_{\vec{k}}^\dagger + c_{\vec{k}}^\dagger \rho c_{\vec{k}} - \rho c_{\vec{k}} c_{\vec{k}}^\dagger \\ & - c_{\vec{k}}^\dagger c_{\vec{k}} \rho) + \tfrac{1}{2} (2 c_{\vec{k}} \rho c_{\vec{k}}^\dagger - c_{\vec{k}}^\dagger c_{\vec{k}} \rho - \rho c_{\vec{k}}^\dagger c_{\vec{k}}) \big] \end{aligned} \tag{A3}$$

is their dissipation into a thermal bath. Here $n_{\mathrm{th}}(\omega_{\vec{k}}) = (e^{\hbar\omega_{\vec{k}}/k_B T} - 1)^{-1}$, k_B is the Boltzmann constant, T is the bath temperature, and $\xi_{\vec{k}}$ are the dissipation rates.

We cover different regimes of the master equation (A1) including the quantum-classical crossover in the form of an equation of motion for the Wigner quasiprobability distribution function:

$$W(\alpha_0,\alpha_0^*,\alpha_{\vec{\mathcal{K}}},\alpha_{\vec{\mathcal{K}}}^*,\alpha_{-\vec{\mathcal{K}}},\alpha_{-\vec{\mathcal{K}}}^*)=\frac{1}{\pi^2}\int d^2z_{-\vec{\mathcal{K}}}\int d^2z_{\vec{\mathcal{K}}}\times\int d^2z_0\,\mathrm{tr}(\rho e^{iz_0^*c_0^\dagger}e^{iz_0c_0}e^{iz_{\vec{\mathcal{K}}}^*c_{\vec{\mathcal{K}}}^\dagger}e^{iz_{\vec{\mathcal{K}}}c_{\vec{\mathcal{K}}}}e^{iz_{-\vec{\mathcal{K}}}^*c_{-\vec{\mathcal{K}}}^\dagger}e^{iz_{-\vec{\mathcal{K}}}c_{-\vec{\mathcal{K}}}})\times e^{-iz_0^*\alpha_0^*}e^{-iz_0\alpha_0}e^{-iz_{\vec{\mathcal{K}}}^*\alpha_{\vec{\mathcal{K}}}^*}e^{-iz_{\vec{\mathcal{K}}}\alpha_{\vec{\mathcal{K}}}}e^{-iz_{-\vec{\mathcal{K}}}^*\alpha_{-\vec{\mathcal{K}}}^*}e^{-iz_{-\vec{\mathcal{K}}}\alpha_{-\vec{\mathcal{K}}}},\quad\text{(A4)}$$

where $z_{\vec{k}}$ and $\alpha_{\vec{k}}$ are complex variables, and $|\alpha_k\rangle$ is the coherent state of mode $\vec{k}$. Following textbook procedures [34,35]

$$\frac{\partial W}{\partial t}=\mathcal{W}_{\mathrm{HO}}+\mathcal{W}_{\mathrm{D}}+\mathcal{W}_{\mathrm{PE}}+\mathcal{W}_{\mathrm{SK}}+\mathcal{W}_{\mathrm{CK}}+\mathcal{W}_{\mathrm{S}},\quad\text{(A5)}$$

where the contributions on the right-hand side represent, respectively, the noninteracting magnons

$$\mathcal{W}_{\mathrm{HO}}=\sum_{k\in\{0,\pm\vec{\mathcal{K}}\}}\left[i\Delta\omega_k\frac{\partial}{\partial\alpha_k}\alpha_k+\mathrm{H.c.}\right]W,\quad\text{(A6)}$$

the dissipation

$$\mathcal{W}_{\mathrm{D}}=\sum_{k\in\{0,\pm\vec{\mathcal{K}}\}}\left[\frac{\xi_k}{2}\frac{\partial}{\partial\alpha_k}\alpha_k+\frac{\xi_k}{2}\frac{\partial}{\partial\alpha_k^*}\alpha_k^*+\xi_k\left(n_{\mathrm{th},k}+\frac{1}{2}\right)\frac{\partial^2}{\partial\alpha_k\partial\alpha_k^*}\right]W,\quad\text{(A7)}$$

the parametric excitation of the Kittel mode

$$\mathcal{W}_{\mathrm{PE}}=\left[-iP_0\frac{\partial}{\partial\alpha_0}\alpha_0^*+\mathrm{H.c.}\right]W,\quad\text{(A8)}$$

the self-Kerr interaction

$$\mathcal{W}_{\mathrm{SK}}=\sum_{k\in\{0,\pm\vec{\mathcal{K}}\}}i\mathcal{D}_{k,k,k,k}\left[2\frac{\partial}{\partial\alpha_k}|\alpha_k|^2\alpha_k+\frac{1}{2}\frac{\partial^3}{\partial\alpha\partial\alpha_k^{*2}}\alpha_k^*+\mathrm{H.c.}\right]W,\quad\text{(A9)}$$

the cross-Kerr interactions

$$\mathcal{W}_{\mathrm{CK}}=\sum_{k\in\{0,\pm\vec{\mathcal{K}}\}}\sum_{k'\in\{0,\pm\vec{\mathcal{K}}\}}i\mathcal{D}_{k,k,k',k'}(1-\delta_{k,k'})\times\left\{\left[\frac{\partial}{\partial\alpha_k}|\alpha_{k'}|^2\alpha_k+\frac{1}{4}\frac{\partial^3}{\partial\alpha_k\partial\alpha_k^*\partial\alpha_{k'}^*}\alpha_{k'}^*\right]+\mathrm{H.c.}\right\}W,\quad\text{(A10)}$$

and the four-magnon interactions that drive the Suhl instability

$$\mathcal{W}_{\mathrm{S}}=i\mathcal{D}_{0,\mathcal{K},0,-\mathcal{K}}\left[2\frac{\partial}{\partial\alpha_0}\alpha_0^*\alpha_{\mathcal{K}}\alpha_{-\mathcal{K}}-\frac{\partial}{\partial\alpha_{-\mathcal{K}}^*}\alpha_0^{*2}\alpha_{\mathcal{K}}+\frac{\partial}{\partial\alpha_{\mathcal{K}}^*}\alpha_0^{*2}\alpha_{-\mathcal{K}}-\frac{1}{4}\frac{\partial^3}{\partial\alpha_0^2\partial\alpha_{-\mathcal{K}}^*}\alpha_{\mathcal{K}}-\frac{1}{4}\frac{\partial^3}{\partial\alpha_0^2\partial\alpha_{\mathcal{K}}^*}\alpha_{-\mathcal{K}}+\frac{1}{2}\frac{\partial^3}{\partial\alpha_0\partial\alpha_{\mathcal{K}}^*\partial\alpha_{-\mathcal{K}}^*}\alpha_0^*+\mathrm{H.c.}\right]W.\quad\text{(A11)}$$

$\partial W/\partial\alpha_k$ is of the order of W when the latter is a peaked function such as a Gaussian. In our system the third-order derivatives in Eqs. (A9)–(A11) are negligibly small since $|\mathcal{D}\alpha_k|\ll\xi_k(n_{\mathrm{th},k}+\frac{1}{2})$. Introducing $x_k=(\alpha_k+\alpha_k^*)/2$ and $p_k=-i(\alpha_k-\alpha_k^*)/2$, the Wigner EOM of Eq. (A5) reduces to the Fokker-Planck equation (summing over repeated indices)

$$\dot{W}(\mathcal{X})=-\frac{\partial}{\partial\mathcal{X}_i}\mathcal{A}_i(\mathcal{X})+\frac{1}{2}\frac{\partial^2}{\partial\mathcal{X}_i\partial\mathcal{X}_j}D_{i,j},\quad\text{(A12)}$$

in the variables $\mathcal{X}=[x_0,p_0,x_{\mathcal{K}},p_{\mathcal{K}},x_{-\mathcal{K}},p_{-\mathcal{K}}]$. $\mathcal{A}_i(\mathcal{X})$ in the first term (drift) follows by straightforward algebra from the first derivatives in Eqs. (A5)–(A10), while the second-order derivatives in Eq. (A7) lead to the second (diffusion) term with $D_{i,j}=\delta_{i,j}\xi_i(n_{\mathrm{th},k}+\frac{1}{2})$. The first and second moments obtained from the FPE can also be obtained as the solution of a set of associated (Ito) stochastic differential equations [34] in which diffusion is obtained by Wiener increments $dW_t=\Xi_i(t)dt$, i.e., the differentials of Markovian Wiener processes governed by the FPE with zero drift and unit diffusion, so

$$d\mathcal{X}_i=\mathcal{A}_idt+\sqrt{\xi_i\left(n_{\mathrm{th},k}+\frac{1}{2}\right)}\Xi_i(t)dt,\quad\text{(A13)}$$

where $\langle\Xi_i(t)\Xi_j(t')\rangle=\delta_{i,j}\delta(t,t')$. Therefore, the *Langevin* equation of motion of the three-partite magnon system reads $\dot{v}=-i[H,v]+\Gamma$, where $v=[x_0,p_0,x_{\vec{\mathcal{K}}},p_{\vec{\mathcal{K}}},x_{-\vec{\mathcal{K}}},p_{-\vec{\mathcal{K}}}]$, and Γ collects fluctuating fields with Gaussian quantum statistics as described above. We solve this six-dimensional Langevin differential equation in real time using the stochastic Runge-Kutta four algorithm. Starting from appropriate initial conditions we update v in time steps of 0.1 ns until a steady state is reached. Figures 8(a) and 8(b) plot the four-magnon scattering parameters $\mathcal{D}$ and $\Delta\omega_{\pm\vec{\mathcal{K}}}$, respectively, as a function of the magnetic field, which we use in our calculations.

APPENDIX B: STEADY STATES FROM QUANTUM MASTER EQUATION

We calculate up to 20 smallest amplitude eigenvalues $\mathcal{E}\geqslant 0$ of the right-hand side of Eq. (A1), in which the $\mathcal{E}=0$ corresponds to the ground -state density matrix ρ_{ss}. We visualize the steady states by the Wigner distribution function $W(x_{0(\vec{\mathcal{K}}_s)},p_{0(\mathcal{K}_s)})=\int\langle x_{0(\vec{\mathcal{K}}_s)}-y/2|\rho_{\mathrm{ss},0(\vec{\mathcal{K}}_s)}|x_{0(\vec{\mathcal{K}}_s)}+y/2\rangle e^{ip_{0(\vec{\mathcal{K}}_s)}y}dy$ of the Kittel ($\vec{\mathcal{K}}_s$) mode, where $|x_{0(\vec{\mathcal{K}}_s)}\pm y/2\rangle$ is the position eigenstate of the Kittel ($\vec{\mathcal{K}}_s$) mode, and $\rho_{\mathrm{ss},0(\vec{\mathcal{K}}_s)}$ is the density matrix after tracing out the $\vec{\mathcal{K}}_s$ (Kittel) mode. The top (bottom) panels of Fig. 4 show $W(x_{0(\vec{\mathcal{K}}_s)},p_{0(\vec{\mathcal{K}}_s)})$ for $H_{\mathrm{ext}}=40$ mT in each of the classical steady-state phases, as indicated by stars of the same color in Fig. 2(a) of the main text. The left and middle panels can be compared with the classical phase space of FP1 and FP2 in Figs. 2(b) and 2(c), respectively. The right panels of Fig. 4 should be compared with the limit cycle region in the classical phase space, e.g., in Fig. 2(c). In the panels of Fig. 4, we used different scale factors $\mathcal{Q}$ such that the distance between the extrema of W is roughly the same.

APPENDIX C: HOPPING FREQUENCY

As explained in the main text, the steady state of the Kittel mode above the parametric instability threshold can be mapped on a degenerate two-level Ising pseudospin that is characterized by two opposite precesssion phases. The transition between these two states is reminiscent of the thermally activated or quantum tunneling of the magnetization in uniformly magnetized nanoparticle or molecular magnets [41–43]. In the absence of the $\pm\vec{\mathcal{K}}$ modes, the physics of the pseudospin of the Kittel mode is similar to a bistable magnetization, where the phase space of the former is the infinite two-dimensional (2D) plane of the Kittel mode harmonic oscillator quasiposition and quasimomentum and the 2D Bloch sphere in the latter. The details of the free energy landscape on the phase spaces determine the competition between tunneling or thermally activated hopping frequencies, but there are some universal features as well. For example, with increasing the parametric excitation power and in the absence of $\pm\vec{\mathcal{K}}$ modes, the pseudospin of the Kittel mode increases while the hopping frequency decreases [see Appendix C 2], similar to the effect of increasing the size of a nanomagnet that leads to decreasing hopping rates. In this work, we control the Kittel mode pseudospin by the mixing with $\pm\vec{\mathcal{K}}$ modes.

1. Number states

We work with a finite basis set $N = N_0 N_{\vec{\mathcal{K}}_s}$, where $N_{0(\vec{\mathcal{K}}_s)}$ is the cutoff number of Fock states of the $0(\vec{\mathcal{K}}_s)$ mode. The Lindblad master equation (A1) can then be written as $\partial_t \mathcal{Z} = \mathcal{L}\mathcal{Z}$, where the Liouvillian $\mathcal{L}$ is an $N^2 \times N^2$ matrix and $\mathcal{Z}$ is the density matrix ρ rearranged into a vector with N^2 elements. The steady state $\mathcal{Z}_{\rm ss}$ is the eigenvector of $\mathcal{L}$ with the eigenvalue $\mathcal{E}_{\rm ss} = 0$. The time-dependent density matrix can be expanded as

$$\mathcal{Z}_{\rm phys}(t) = \sum_i \mathcal{M}_i e^{\mathcal{E}_i t}\mathcal{Z}_i, \tag{C1}$$

where the sum runs over the N^2 eigenstates, and $\mathcal{M}_i = \mathcal{Z}_i^T \mathcal{Z}_{\rm phys}(0)$. $\forall i \neq {\rm ss} \Longrightarrow {\rm Re}\mathcal{E}_i < 0$ and $\lim_{t\to\infty}\mathcal{Z}_{\rm phys} = \mathcal{Z}_{\rm ss}$.

We may model the magnon parametron by two coherent states of a harmonic oscillator separated by a high barrier in the position-momentum phase space. An eigenvalue $\mathcal{E}_{\rm tnl}$ that satisfies ${\rm Im}\mathcal{E}_{\rm tnl} = 0$ is then associated with hopping. Since this rate is small compared to other fluctuations and so is $|\mathcal{E}_{\rm tnl}|$ [40], we can calculate it accurately with a small basis set. We analyze the associated tunneling eigenvector $\mathcal{Z}_{\rm tnl}$ starting from an initial coherent state in one of the two Ising valleys $\mathcal{Z}_{\rm phys}$ $(t = 0)$. To leading order in the interaction $\mathcal{Z}_{\rm phys}(0) \approx \mathcal{Z}_{\rm ss} + \mathcal{M}_{\rm tnl}\mathcal{Z}_{\rm tnl}$ and $\mathcal{Z}_{\rm phys}(\infty) \approx \mathcal{Z}_{\rm ss}$. It is convenient here to work with the non-negative Husimi function $Q(\alpha) = \langle\alpha|\rho_{\rm phys}|\alpha\rangle/\pi > 0$, where $|\alpha\rangle$ is a coherent state and the $N^2 \times N^2$ density matrix $\rho_{\rm phys}$ contains all elements of the vector $\mathcal{Z}_{\rm phys}$. Figure 3 shows that above the threshold and at long times the two valleys become symmetrically occupied with two identical maxima of $Q(\alpha)$ representing two mirror-symmetric coherent states. The latter corresponds to $Q(\alpha, \infty)$ for $\mathcal{Z}_{\rm phys}(\infty) = \mathcal{Z}_{\rm ss}$, whereas the initial $Q(\alpha, 0)$ corresponding to $\mathcal{Z}_{\rm phys}(0)$, which we assumed is a coherent state at one of the valleys, has only one peak at that valley. The decomposition $\mathcal{Z}_{\rm phys}(0) = \mathcal{Z}_{\rm ss} + \mathcal{M}_{\rm tnl}\mathcal{Z}_{\rm tnl}$ implies that the overlap of $\mathcal{Z}_{\rm tnl}$ with two coherent states at the two valleys should have the opposite sign in order to cancel $\mathcal{Z}_{\rm ss}$ at one of the valleys and add to it at the other valley, for $Q(\alpha, 0)$ to have only one peak at one of the valleys and the integration of $Q(\alpha, 0)$ over the phase space to remain equivalent to that of $Q(\alpha, \infty)$.

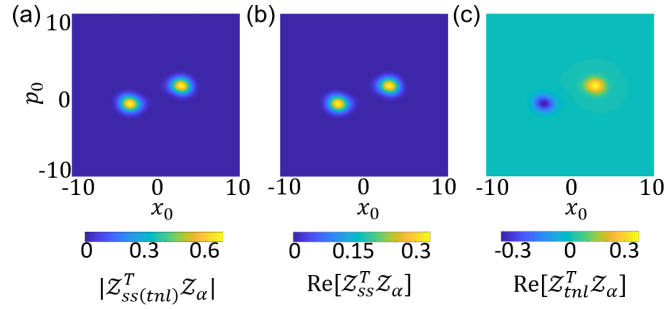

FIG. 5. (a) The modulus of the overlap of the Liouvillian eigenvectors $\mathcal{Z}_{\rm ss(tnl)}$ with the vector corresponding to the density matrix of the coherent state $\mathcal{Z}_\alpha$, $\alpha = x_0 + ip_0$, i.e., $|\mathcal{Z}^T_{\rm ss(tnl)}\mathcal{Z}_\alpha|$. (b) ${\rm Re}[\mathcal{Z}^T_{\rm ss}\mathcal{Z}_\alpha]$. (c) ${\rm Re}[\mathcal{Z}^T_{\rm tnl}\mathcal{Z}_\alpha]$.

Let us first ignore $\vec{\mathcal{K}}_s$ and only consider the parametrically excited Kittel mode with self-Kerr nonlinearity. Figure 5(a) shows the absolute value of the overlap $|\mathcal{Z}^T_{\rm ss}\mathcal{Z}_\alpha|$ between the steady state with the elements of the coherent-state density matrix $|\alpha\rangle\langle\alpha|$ arranged into the vector $\mathcal{Z}_\alpha$, where $\alpha = x_0 + ip_0$. $|\mathcal{Z}^T_{\rm tnl}\mathcal{Z}_\alpha| = |\mathcal{Z}^T_{\rm ss}\mathcal{Z}_\alpha|$, as expected. Figure 5(b) shows that ${\rm Re}\,\mathcal{Z}^T_{\rm ss}\mathcal{Z}_\alpha$ is symmetric with respect to $(x_0 = 0$ and $p_0 = 0)$, while Fig. 5(c) indicates that ${\rm Re}\,\mathcal{Z}^T_{\rm tnl}\mathcal{Z}_\alpha$ is antisymmetric (and the same holds for the imaginary parts).

When the Suhl instability of the Kittel mode parametron drives the $\vec{\mathcal{K}}_s$ mode, there are two tunneling eigenvalues $\mathcal{E}_{\rm tnl,1(2)}$. The Kittel mode hopping frequency is $\mathcal{F} = -\mathcal{E}_{\rm tnl,1}$ when $|\mathcal{Z}^T_{\rm tnl,1}\mathcal{Z}_\alpha| = |\mathcal{Z}^T_{\rm ss}\mathcal{Z}_\alpha|$ $\forall\alpha$, otherwise $\mathcal{F} = -\mathcal{E}_{\rm tnl,2}$.

2. Kittel mode parametric oscillator

Here, we address the parametrically driven Kittel mode with the finite self-Kerr nonlinearity K_0 but without interactions with other magnons, equivalent to a Duffing oscillator. The Fokker-Planck equation for the Wigner distribution function to leading order in the derivatives with respect to coherent states α and α^* then reduces to

$$\dot{W}(\alpha, \alpha^*) = \frac{\partial}{\partial\alpha}[\alpha + i\alpha^*(\mu + 2K_0\alpha^2)] + \frac{1}{2}\frac{\partial^2}{\partial\alpha\partial\alpha^*}(1 + 2n_{\rm th}) + {\rm H.c.}, \tag{C2}$$

where $K_0 = 2\mathcal{Q}\mathcal{D}_{0,0,0,0}/\xi_0$ and $\mu = 2P_0/\xi_0$. With $\alpha = x_0 + ip_0$,

$$\dot{W}(x_0, p_0) = \left[-\frac{\partial}{\partial\mathcal{X}_i}\mathcal{A}_i + \frac{1}{2}\frac{\partial^2}{\partial\mathcal{X}_i\partial\mathcal{X}_j}D_{i,j}\right]W(x_0, p_0), \tag{C3}$$

where $\mathcal{X} = [x_0, p_0]$, $\mathcal{A}_1 = -[x_0 - 4K_0(x_0^2 + p_0^2) + 2\mu p_0]$, $\mathcal{A}_2 = -[p_0 + 4K_0(x_0^2 + p_0^2) + 2\mu x_0]$, and $D_{i,j} = \delta_{i,j}(1 + 2n_{\rm th})/2$. The maxima of W are the steady-state mean-field amplitudes $\alpha_0 = |\alpha_0|e^{i\phi_0}$ that follow from the first term and

its conjugate (drift) of Eq. (C2),

$$i\mu\alpha_0^* + \alpha_0 + 2iK_0|\alpha_0|^2\alpha_0 = 0,$$
$$-i\mu\alpha_0 + \alpha_0^* - 2iK_0|\alpha_0|^2\alpha_0^* = 0. \quad \text{(C4)}$$

Hence, $|\alpha_0|^2 = \sqrt{\mu^2-1}|K_0|/2$, and $2\phi_0 = \arg[-K_0\sqrt{\mu^2-1}/\mu|K_0| + i/\mu]$.

In the steady state [34,35]

$$A_i W = \frac{1}{2}\frac{\partial}{\partial \mathcal{X}_i} D_{i,j} W. \quad \text{(C5)}$$

Assuming a solution of the form $W(x_0, p_0) = \mathcal{N} e^{-\Phi(x_0,p_0)}$, where $\mathcal{N}$ is the normalizing constant, we get

$$-\frac{\partial \Phi}{\partial \mathcal{X}_i} = 2D^{-1}_{i,j}\left[A_j - \frac{1}{2}\frac{\partial D_{j,l}}{\partial \mathcal{X}_l}\right], \quad \text{(C6)}$$

where Φ is a proper potential with $\partial^2\Phi/\partial x_0\partial p_0 = \partial^2\Phi/\partial p_0\partial x_0$, which ensures that the solutions of Eq. (C6) do not depend on the path of integration, i.e.,

$$\Phi = -\int_0^x \frac{\partial \Phi}{\partial \mathcal{X}_i} d\mathcal{X}_i.$$

Strictly speaking $\partial^2\Phi/\partial x_0\partial p_0 = 4[-4K_0(3p_0^2 + x_0^2) + 2\mu]/(1+2n_{\rm th})$ and $\partial^2\Phi/\partial p_0\partial x_0 = 4[4K_0(3x_0^2 + p_0^2) + 2\mu]/(1+2n_{\rm th})$ are not equal. However, in the region between the two minima $(x_{0,m}, p_{0,m})$, $|4K_0|(3x_{0,m}^2 + p_{0,m}^2) \ll 2\mu$ and $|4K_0|(x_{0,m}^2 + 3p_{0,m}^2) \ll 2\mu$. For very small $\mu > 1$ above the threshold $\phi_{0,m} \approx \pi/4$, and $(x_{0,m}, p_{0,m}) = (0, \pm|\alpha_0|)$. Therefore, $12|K_0\alpha_0|^2 = 6\sqrt{\mu^2-1} \ll 2\mu$, i.e., $1 < \mu \ll \sqrt{9/8}$, approximately satisfies the potential conditions. The transition time in this potential barrier approximation [40,44] is obtained as

$$\tau = \frac{2\pi}{\xi_0}\left[\frac{\Phi_{x_0x_0}(0,0)}{\Phi_{x_0x_0}(0,|\alpha_0|)\Phi_{p_0p_0}(0,|\alpha_0|)\Phi_{p_0p_0}(0,0)}\right]^{1/2} \times \exp\left[\Phi(0,|\alpha_0|) - \Phi(0,0)\right], \quad \text{(C7)}$$

where $\Phi_{\mathcal{X}_i\mathcal{X}_i} = \partial^2\Phi/\partial\mathcal{X}_i^2$. Hence,

$$\tau = \frac{\pi(1+2n_{\rm th})}{2\xi_0}\exp\left[\frac{\sqrt{\mu^2-1}}{(1+2n_{\rm th})|K_0|}\right]. \quad \text{(C8)}$$

Kinsler and Drummond [40] studied the transition frequency of a parametron in the presence of nonlinear damping rather than self-Kerr nonlinearity, at zero temperature. Because of the similarity of the steady states governed by either the self-Kerr interaction or the nonlinear damping (see below), and the validity of the analytic treatment for a large μ interval in the latter case, we extend the analysis in Ref. [40] to nonzero temperatures through the Lindblad operator,

$$L_{\rm NL} = \xi_{\rm NL}(n_{\rm th}+1)\left(2c_0^2\rho c_0^{\dagger 2} - c_0^{\dagger 2}c_0^2\rho - \rho c_0^{\dagger 2}c_0^2\right) + \xi_{\rm NL}n_{\rm th}\left(2c_0^{\dagger 2}\rho c_0^2 - c_0^2c_0^{\dagger 2}\rho - \rho c_0^2c_0^{\dagger 2}\right), \quad \text{(C9)}$$

where $\xi_{\rm NL}$ is the nonlinear dissipation parameter. Nonlinear dissipation should exist under parametric excitation conditions due to photon dissipation and four-magnon scattering to thermal magnons, but in contrast to the self-Kerr term, its value for YIG is unkown. For simplicity, we set $K_0 = 0$ and assume an imaginary parametric excitation, $iP_0c_0^\dagger c_0^\dagger + \text{H.c.}$, where P_0 and thereby $\mu = 2P_0/\xi_0$ are real, i.e., a phase shift of the drive by $\pi/2$ relative to the global phase reference. The Wigner function then solves

$$\frac{dW}{dt} = \left\{\frac{\partial}{\partial\alpha}\left[\alpha - \alpha^*(\mu - g_{\rm NL}\alpha^2)\right] + \frac{(1+2n_{\rm th})}{2}\frac{\partial^2}{\partial\alpha\partial\alpha^*}(1 + g_{\rm NL}\alpha\alpha^*) + \text{H.c.}\right\}W, \quad \text{(C10)}$$

where $g_{\rm NL} = 4\xi_{\rm NL}/\xi_0$. In terms of (x_0, p_0), where $\alpha = x_0 + ip_0$, Eq. (C10) can be written in the form of Eq. (C3), where $A_1 = -x_0(1 + g_{\rm NL}x_0^2 - \mu)$, $A_2 = -p_0(1 + g_{\rm NL}p_0^2 + \mu)$, $D_{11} = (1+2n_{\rm th})(1+2g_{\rm NL}x_0^2)/4$, and $D_{22} = (1+2n_{\rm th})(1+2g_{\rm NL}p_0^2)/4$. The resulting 2D FPE does not have a potential solution, because $\partial^2\Phi/\partial x_0\partial p_0 \neq \partial^2\Phi/\partial p_0\partial x_0$ [see Eq. (C6)]. However, the states always relax towards $p_0 = 0$ because A_2 has the sign opposite to that of p_0. The FPE for $p_0 = 0$ is only a function of x_0 [40]:

$$\frac{dW_{\rm 1D}}{dt} = \left\{\frac{\partial}{\partial x_0}\left[x_0\left(1 + g_{\rm NL}x_0^2 - \mu\right)\right] + \frac{1}{4}\frac{\partial^2}{\partial x_0^2}\left[(1+2n_{\rm th})\left(1+2g_{\rm NL}x_0^2\right)\right]\right\}. \quad \text{(C11)}$$

All 1D FPE equations have potential solutions [35], and Eqs. (C6) and (C11) lead to

$$\Phi(x_0) = \frac{1}{(1+2n_{\rm th})}\left[x_0^2 - \frac{2R+1}{2g_{\rm NL}}\ln\left(2g_{\rm NL}x_0^2 + 1\right)\right], \quad \text{(C12)}$$

where $R = \mu - g_{\rm NL}(1+2n_{\rm th}) - 1$. The extrema of Φ_{x_0} are at $x_{0,s} = 0$ (saddle point) and $x_{0,m} = \pm\sqrt{R/g_{\rm NL}}$ (the two minima). The transition time between the two minima is

$$\tau = \frac{2\pi}{\xi_0}\left[\frac{1}{\Phi_{x_0x_0}(x_{0,m})\Phi_{x_0x_0}(x_{0,s})}\right]^{1/2} \times \exp\left[\Phi(x_{0,s}) - \Phi(x_{0,m})\right], \quad \text{(C13)}$$

which with Eq. (C12) leads to

$$\tau = \frac{\pi}{2\xi_0}\left[\frac{(1+2n_{\rm th})^2(1+2R)}{2R^2}\right]^{1/2} \times \exp\left\{\frac{1}{2g_{\rm NL}(1+2n_{\rm th})}\left[(2R+1)\ln(2R+1) - 2R\right]\right\}. \quad \text{(C14)}$$

In Fig. 6(a), we compare the hopping frequency $\mathcal{F}$ from a numerical solution of the master equation corresponding to either $g_{\rm NL}$ or K_0 being finite, with the analytical equations (C8) and (C14), respectively, for $n_{\rm th} = 0$ and a scaling coefficient $\mathcal{Q} = 5\times10^8$ of the four-magnon scattering coefficients $\mathcal{D} \to \mathcal{Q}\mathcal{D}$ that reduces the Hilbert space to a manageable size. We illustrate the results by choosing $g_{\rm NL} = |K_0|$. Figure 6(a) shows that Eq. (C14) approximately agrees with numerical calculation [40], whereas Eq. (C8) is too small for $\mu > 1$, i.e., above the parametric pumping threshold, because the assumption of small μ is not valid anymore. We may improve Eq. (C14) by adopting a distance between the two minima for the nonlinear damping that equals that of the self-Kerr

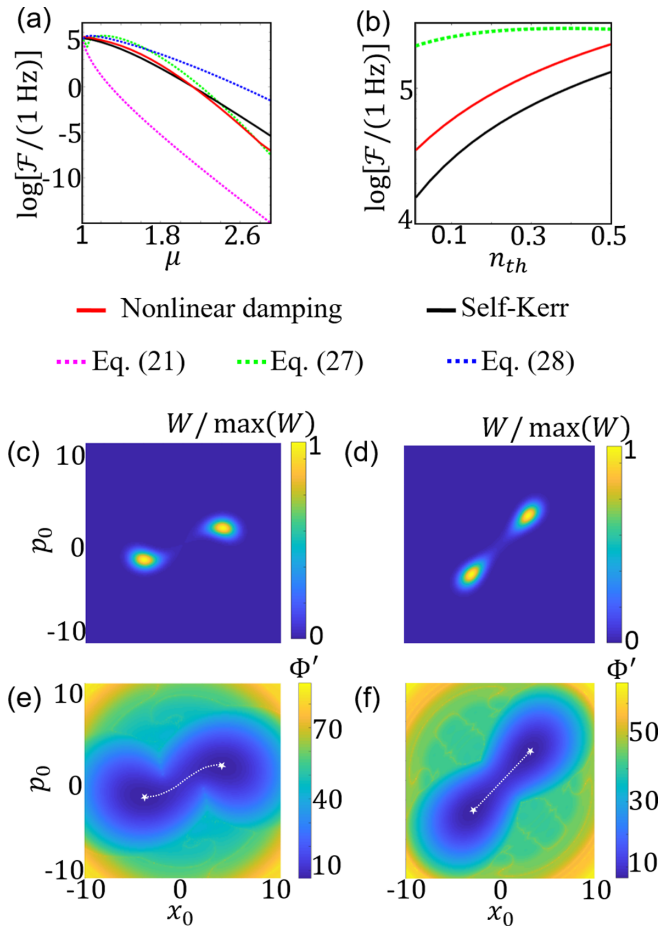

FIG. 6. (a) The dependence of the tunneling frequency $\mathcal{F}$ on μ from quantum calculations for nonlinear damping and self-Kerr nonlinearity. $\mathcal{F}$ values from analytical equations (C8), (C14), and (C15) are also shown. $n_{\rm th} = 0$. (b) The dependence of $\mathcal{F}$ on $n_{\rm th}$ for $\mu = 1.4$. In panels (a) and (b), $\mathcal{Q} = 5 \times 10^8$. (c) and (d) The Wigner function for self-Kerr nonlinearity and nonlinear damping, respectively, while $\mu = 1.4$. (e) and (f) The quasipotential, $\Phi' = -\ln W$, corresponding to panels (c) and (d). The stars are the minima of Φ' and the dashed lines are along the minimal gradient path. In panels (c)–(f), $\mathcal{Q} = 5 \times 10^8$. In panels (a)–(f), $H_{\rm ext} = 40$ mT.

nonlinearity, i.e., $(\mu' - 1)/g_{\rm NL} = \sqrt{\mu^2 - 1}/2|K_0|$,

$$\tau = \frac{\pi}{2\xi_0}\left[\frac{(1+2n_{\rm th})^2(1+2R')}{2R'^2}\right]^{1/2} \times \exp\left\{\frac{1}{2g_{\rm NL}(1+2n_{\rm th})}[(2R'+1)\ln(2R'+1) - 2R']\right\}, \tag{C15}$$

where $R' = \sqrt{\mu^2 - 1}/2 + 1 - g_{\rm NL}(1 + 2n_{th}) - 1$. The blue dashed line in Fig. 6(a) shows that the transition frequency from Eq. (C15) now overestimates $\mathcal{F}$ for the self-Kerr nonlinearity and can be used as an analytical upper bound when $n_{\rm th} = 0$.

Figure 6(b) shows the dependence of $\mathcal{F}$ on $n_{\rm th}$ for $\mu = 1.4$ and $\mathcal{Q} = 5 \times 10^8$ for both cases of self-Kerr and nonlinear damping. Figure 6(b) shows that, with increasing temperature, $\mathcal{F}$ increases as expected. $\mathcal{F}$ according to Eq. (C14) monotonically increases with temperature up to $n_{\rm th} \approx 0.5$ and is larger than the numerical calculations [see the green dashed line in Fig. 6(b)]. Figure 6(b) is for $\mathcal{Q} = 5 \times 10^8$, which means that the potential is 5×10^8 times shallower than that of the physical ($\mathcal{Q} = 1$) case [see Eq. (C12)]. Therefore, we can estimate that $n_{\rm th} = 0.5$ when $\mathcal{Q} = 5 \times 10^8$ corresponds to $0.5 \times 5 \times 10^8 \sim 2.5 \times 10^8$, i.e., $T \approx 10^7$ K when $\mathcal{Q} = 1$. We confirm that for any μ, when $\mathcal{Q} = 5 \times 10^8$, and $n_{\rm th} < 0.5$, $\mathcal{F}$ from Eq. (C15) is larger than the numerical calculation for the case of self-Kerr nonlinearity. Therefore, for the physical case, Eq. (C15) provides a reliable upper bound of $\mathcal{F}$ for $T < 10^7$ K and every value of μ.

Figures 6(e) and 6(f) show the (quasi)potential $\Phi' = -\ln W$, corresponding to Figs. 6(c) and 6(d), respectively. The white stars indicate the minima of Φ', and the white dashed line connects the two minima through the minimal gradient path that governs the transition. The latter line is not straight for the self-Kerr nonlinearity in contrast to that for nonlinear damping, supporting the validity of the 1D assumption leading to Eq. (C11). Apart from the twist in the quasipotential of Fig. 6(e), it is approximately the same as that of Fig. 6(f), leading to the similar scale of $\mathcal{F}$ for self-Kerr nonlinearity and nonlinear damping. In conclusion, while a hypothetical, substantial nonlinear damping should affect the numbers but not the phenomenology and can be captured by rescaling the Kerr constant.

APPENDIX D: SUHL INSTABILITY AND BIFURCATION OF THE LIMIT CYCLES

In Appendix C 2, we discussed the hopping frequency $\mathcal{F}$ of the Kittel mode parametron in the absence of interactions with the $\pm\vec{K}$ pair. We showed in the main text that for P_0 above the Suhl instability that leads to the decay into finite-momentum magnon pairs the transition rate increases substantially when the steady state is a limit cycle (LC). Here, we discuss the LC trajectories as a function of P_0 up to just below the jump in $\mathcal{F}$. Figure 7(a) presents our results for the steady states as a function of P_0/ξ_0 (see also Fig. 2), for $H_{\rm ext} = 40$ mT, and indicates the respective values of P_0/ξ_0 corresponding to Figs. 7(b)–7(g) in increasing order. In Figs. 7(b)–7(g), we assumed $T = 0$ and an initial random (x_0, p_0) near the origin. The black trajectories are from $t = 0$ to $t = 40$ μs, whereas the purple ones are the steady-state trajectories from $t = 30$ μs to $t = 40$ μs. Figure 7(b) is the fixed-point FP1 steady state below the Suhl instability. Figure 7(c) is the fixed-point FP2 steady state generated by the Suhl instability. The Ising spin states of FP1 and FP2 are extremely stable, with astronomically small hopping frequencies.

Figure 7(d) corresponds to a microwave power just above the bifurcation to a LC steady state. Initially, the LC has a small amplitude that increases with P_0/ξ_0 to develop a pronounced butterfly shape [see Fig. 7(e)]. For even larger P_0/ξ_0, the limit cycle bifurcates. In the steady state in Fig. 7(f) we observe two LC butterflies and we observe four LC butterflies in Fig. 7(g). The increase in the LC radius and its multiplying indicates a shallower potential trench that confines the dynamics and a much broader probability distribution that is definitely not Gaussian. A shallower potential well or trench implies an

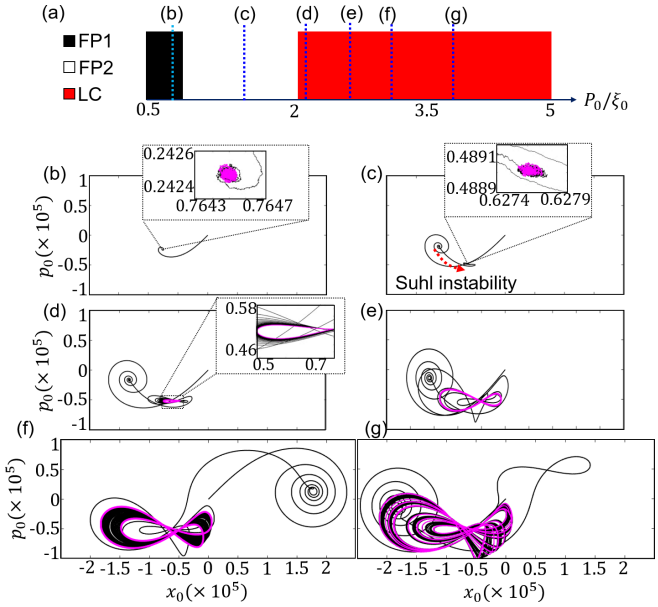

FIG. 7. (a) The dynamical steady states of the magnetic dot calculated as a function of P_0/ξ_0, for $H_{\rm ext} = 40$ mT. The blue dashed lines indicate P_0/ξ_0 values that correspond to the time traces plotted in panels (b)–(g). (b) $P_0/\xi_0 = 0.86$, FP1. (c) $P_0/\xi_0 = 1.51$, FP2. The red dashed arrow indicates the Suhl instability due to parametric pumping. (d) $P_0/\xi_0 = 2.06$, LC. (e) $P_0/\xi_0 = 2.34$, LC. (f) $P_0/\xi_0 = 2.89$, LC. (g) $P_0/\xi_0 = 3.81$, LC. In panels (b)–(g), the black trajectories are from $t = 0$ to $t = 40$ μs, and the purple trajectories are from $t = 30$ μs to $t = 40$ μs. The insets in panels (b)–(d) are zooms of the main panels.

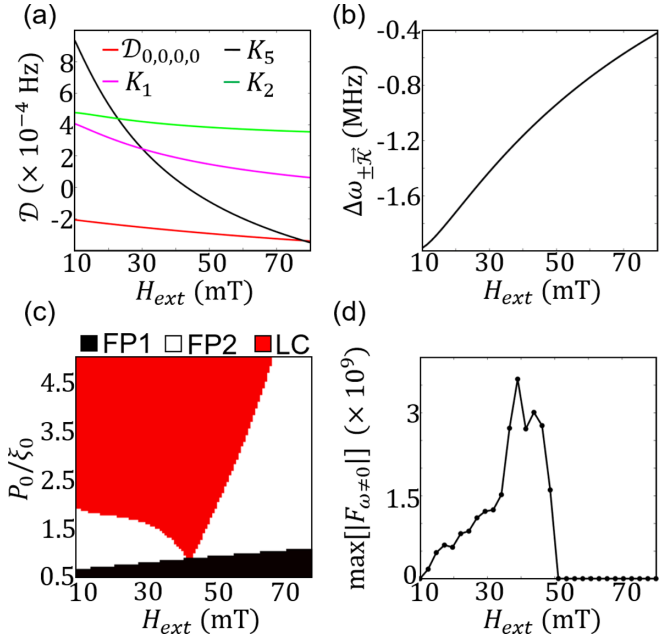

FIG. 8. (a) The dependence of four-magnon scattering coefficients relevant to the dynamics on $H_{\rm ext}$. (b) The dependence of $\Delta\omega_{\pm\vec{\mathcal{K}}}$ on $H_{\rm ext}$. (c) An analytical phase diagram [see Fig. 2(a)]. (d) The $H_{\rm ext}$ dependence of the peak of Fourier transform of $x_0(t)$, F_ω, at any $\omega \neq 0$, for $P_0/\xi_0 = 3.5$ [see Figs. 2(a) and 3(c)].

increase in the hopping over the saddle point between the two Ising spin states.

Next, we discuss the field dependence of the steady-state phase diagram of Fig. 2(a) and the associated Ising spin flip rates. At a fixed P_0, the steady states are governed by the four-magnon scattering coefficients $\mathcal{D}$ and $\Delta\omega_{\pm\vec{\mathcal{K}}}$, which in turn depend on $H_{\rm ext}$. Figure 8(a) shows the dependence of $\mathcal{D}_{0,0,0,0}$, $K_1 = \mathcal{D}_{0,0,\pm\vec{\mathcal{K}},\pm\vec{\mathcal{K}}}$, $K_2 = \mathcal{D}_{0,\vec{\mathcal{K}},0,-\vec{\mathcal{K}}}$, and $K_5 = 2K_3 + K_4$ on $H_{\rm ext}$, where $K_3 = \mathcal{D}_{\pm\vec{\mathcal{K}},\pm\vec{\mathcal{K}},\pm\vec{\mathcal{K}},\pm\vec{\mathcal{K}}}$ and $K_4 = \mathcal{D}_{\pm\vec{\mathcal{K}},\pm\vec{\mathcal{K}},\mp\vec{\mathcal{K}},\mp\vec{\mathcal{K}}}$. Figure 8(b) shows the dependence of $\Delta\omega_{\pm\vec{\mathcal{K}}}$ on $H_{\rm ext}$. As we discussed in the main text, the boundary of FP1 and FP2 [the green line in Fig. 2(a)] is the Suhl instability threshold. According to Eq. (4) of the main text,

$$|\alpha_{0,\rm Suhl}|^2 = \frac{1}{K_2^2 - K_1^2}\Big[\Delta\omega_{\pm\vec{\mathcal{K}}}K_1 + \sqrt{\Delta\omega_{\pm\vec{\mathcal{K}}}{}^2K_1^2 + (K_2^2 - K_1^2)\big(\xi_0^2/4 + \Delta\omega_{\pm\vec{\mathcal{K}}}{}^2\big)}\Big]. \tag{D1}$$

For $\xi_0 = 5$ MHz, $|\alpha_{0,\rm Suhl}|^2 \approx \xi_0/2\sqrt{K_2^2 - K_1^2}$ decreases by a factor of $\sim 1/1.3$ when increasing $H_{\rm ext}$ from 10 to 80 mT, while $|\alpha_0|^2 \propto 1/|\mathcal{D}_{0,0,0,0}|$ decreases by a factor of $\sim 1/1.7$. The P_0 needed to drive the Suhl instability, therefore, increases slightly by a factor of $\sim 1.7/1.3$ in the field interval, as does the green line in Fig. 2(a).

We proceed by the rather rough approximation that beyond the Suhl instability the Kittel mode mean field $\alpha_0 = |\alpha_0|e^{i\phi_0}$ is constant with

$$|\alpha_0|^2 = \frac{1}{2|\mathcal{D}_{0,0,0,0}|}\sqrt{P_0^2 - \left(\frac{\xi}{2}\right)^2},$$
$$\phi_0 = -\arg\left[\frac{-i}{P_0}\left(\frac{\xi}{2} + 2i\mathcal{D}_{0,0,0,0}|\alpha_0|^2\right)\right]\Big/2, \tag{D2}$$

which is the steady state of the self-Hamiltonian $(P_0c_0^\dagger c_0^\dagger + \text{H.c.}) + \mathcal{D}_{0,0,0,0}c_0^\dagger c_0 c_0^\dagger c_0$. The mean field $\alpha_{\vec{\mathcal{K}}_s}$ is then the steady state of the effective Hamiltonian $\Delta'\omega_{\vec{\mathcal{K}}_s}c_{\vec{\mathcal{K}}_s}^\dagger c_{\vec{\mathcal{K}}_s} + (K_2\alpha_0^2 c_{\vec{\mathcal{K}}_s}^\dagger c_{\vec{\mathcal{K}}_s}^\dagger + \text{H.c.}) + K_5 c_{\vec{\mathcal{K}}_s}^\dagger c_{\vec{\mathcal{K}}_s} c_{\vec{\mathcal{K}}_s}^\dagger c_{\vec{\mathcal{K}}_s}$, where $\Delta'\omega_{\vec{\mathcal{K}}_s} = \Delta\omega_{\vec{\mathcal{K}}_s} + K_1|\alpha_0|^2$. Here, $K_1 = \mathcal{D}_{0,0,\pm\vec{\mathcal{K}},\pm\vec{\mathcal{K}}}$, $K_2 = \mathcal{D}_{0,\vec{\mathcal{K}},0,-\vec{\mathcal{K}}}$, $K_5 = 2K_3 + K_4$, $K_3 = \mathcal{D}_{\pm\vec{\mathcal{K}},\pm\vec{\mathcal{K}},\pm\vec{\mathcal{K}},\pm\vec{\mathcal{K}}}$, and $K_4 = \mathcal{D}_{\pm\vec{\mathcal{K}},\pm\vec{\mathcal{K}},\mp\vec{\mathcal{K}},\mp\vec{\mathcal{K}}}$, and

$$\alpha_{\vec{\mathcal{K}}_s} = |\alpha_{\vec{\mathcal{K}}_s}|e^{i\phi_{\vec{\mathcal{K}}_s}},\ |\alpha_{\vec{\mathcal{K}}_s}|^2 = \frac{1}{2|K_5|}\sqrt{K_2^2|\alpha_0|^4 - \left(\frac{\xi}{2}\right)^2} - \Delta'\omega_{\vec{\mathcal{K}}_s},$$
$$\phi_{\vec{\mathcal{K}}_s} = \arg\left[\frac{-i}{2\alpha_0^2}\left(-\frac{\xi}{2} - 2iK_5|\alpha_{\vec{\mathcal{K}}_s}|^2 - i\Delta'\omega_{\vec{\mathcal{K}}_s}\right)\right]/2. \tag{D3}$$

We can estimate the boundary between FP2 and LC phases by the approximations for α_0 and $\alpha_{\vec{\mathcal{K}}_s}$ in Eqs. (D2) and (D3) above the threshold. The transition for a limit cycle by the mean-field term $K_1\alpha_0^*\alpha_{\vec{\mathcal{K}}_s}^*\delta c_0\delta c_{\vec{\mathcal{K}}_s} + \text{H.c.}$ requires that

$$|K_1\alpha_{0,\rm LC}\alpha_{\vec{\mathcal{K}}_s,\rm LC}| = \xi_0/2, \tag{D4}$$

where $\alpha_{0,\rm LC}$ and $\alpha_{\vec{\mathcal{K}}_s,\rm LC}$ are the mean fields at the FP2 to LC transition. For the same magnetic-field

interval and fixed P_0, $|\alpha_0|^2 \propto 1/|\mathcal{D}_{0,0,0,0}|$ decreases by a factor of $\sim 1/1.7$. In $|\alpha_{\vec{\mathcal{K}}_s}|^2 \propto (K_2+K_1)|\alpha_0|^2/|K_5| \propto (K_2+K_1)/|K_5||\mathcal{D}_{0,0,0,0}|$, $(K_2+K_1)/\mathcal{D}_{0,0,0,0}|$ decreases by a factor of ~ 0.3, while $|K_5|$ decreases to zero at around 40 mT and then increases to ~ 0.5 times the initial value, at 80 mT. K_1 monotonically decreases by a factor of $\sim 1/8$ with increasing H_{ext} in the same range. Therefore, P_0 corresponding to $|K_1\alpha_{0,\text{LC}}\alpha_{\vec{\mathcal{K}}_s,\text{LC}}|$ has a minimum at $H_{\text{ext}} \sim 40$ mT and is larger by a factor of ~ 8 for $H_{\text{ext}} = 80$ mT than $H_{\text{ext}} = 10$ mT. Figure 8(c) shows the boundaries between FP2, FP1, and LC as calculated from Eq. (D4) and Eqs. (D2) and (D3) and captures the main features of the numerically exact phase diagram of Fig. 2(a). The differences such as the strong drop of the FP2 | LC boundary at intermediate fields are a consequence of the rough mean-field approximation.

We expect that for fixed P_0 beyond the LC transition the LC oscillation amplitudes would be enhanced at $H_{\text{ext}} \sim 40$ mT. This is indeed consistent with the Ising spin hopping rate $\mathcal{F}$ in Figs. 3(c) and 3(d). F_ω, the Fourier transform of $x_0(t)$, may help to elucidate the correlation between the LC oscillation amplitude and $\mathcal{F}$ since a peaked F_ω indicates that the steady state is a limit cycle. Figure 8(d) shows the dependence of this peak amplitude, $\max(|F_{\omega\neq 0}|)$, on H_{ext} that confirms the expectations.

[1] M. Yamaoka, C. Yoshimura, M. Hayashi, T. Okuyama, H. Aoki, and H. Mizuno, A 20k-spin Ising Chip to solve combinatorial optimization problems with CMOS annealing, IEEE J. Solid-State Circuits **51**, 303 (2016).

[2] T. Inagaki, K. Inaba, R. Hamerly, K. Inoue, Y. Yamamoto, and H. Takesue, Large-scale Ising spin network based on degenerate optical parametric oscillators, Nat. Photonics **10**, 415 (2016).

[3] T. Inagaki, Y. Haribara, K. Igarashi, T. Sonobe, S. Tamate, T. Honjo, A. Marandi, P. L. McMahon, T. Umeki, K. Enbutsu, O. Tadanaga, H. Takenouchi, K. Aihara, K.-I. Kawarabayashi, K. Inoue, S. Utsunomiya, and H. Takesue, A coherent Ising machine for 2000-node optimization problems, Science **354**, 603 (2016).

[4] P. L. McMahon, A. Marandi, Y. Haribara, R. Hamerly, C. Langrock, S. Tamate, T. Inagaki, H. Takesue, S. Utsunomiya, K. Aihara, R. L. Byer, M. M. Fejer, H. Mabuchi, and Y. Yamamoto, A fully programmable 100-spin coherent Ising machine with all-to-all connections, Science **354**, 614 (2016).

[5] D. Pierangeli, G. Marcucci, and C. Conti, Large-Scale Photonic Ising Machine by Spatial Light Modulation, Phys. Rev. Lett. **122**, 213902 (2019).

[6] W. A. Borders, A. Z. Pervaiz, S. Fukami, K. Y. Camsari, H. Ohno, and S. Datta, Integer factorization using stochastic magnetic tunnel junctions, Nature (London) **573**, 390 (2019).

[7] M. A. Nielsen and I. L. Chuang, *Quantum Computation and Quantum Information* (Cambridge University, Cambridge, England, 2009).

[8] D. P. DiVincenzo, Quantum computation, Science **270**, 255 (1995).

[9] T. Albash and D. A. Lidar, Adiabatic quantum computation, Rev. Mod. Phys. **90**, 015002 (2018).

[10] E. Farhi, J. Goldstone, S. Gutmann, J. Lapan, A. Lundgren, and D. Preda, A quantum adiabatic evolution algorithm applied to random instances of an NP-complete problem, Science **292**, 472 (2001).

[11] S. Boixo, T. F. Rønnow, S. V. Isakov, Z. Wang, D. Wecker, D. A. Lidar, J. M. Martinis, and M. Troyer, Evidence for quantum annealing with more than one hundred qubits, Nat. Phys. **10**, 218 (2014).

[12] M. W. Johnson, M. H. S. Amin, S. Gildert, T. Lanting, F. Hamze, N. Dickson, R. Harris, A. J. Berkley, J. Johansson, P. Bunyk, E. M. Chapple, C. Enderud, J. P. Hilton, K. Karimi, E. Ladizinsky, N. Ladizinsky, T. Oh, I. Perminov, C. Rich, M. C. Thom *et al.* Quantum annealing with manufactured spins, Nature (London) **473**, 194 (2011).

[13] T. Makiuchi, T. Hioki, Y. Shimazu, Y. Oikawa, N. Yokoi, S. Daimon, and E. Saitoh, Parametron on magnetic dot: Stable and stochastic operation, Appl. Phys. Lett. **118**, 022402 (2021).

[14] I. Mahboob, H. Okamoto, and H. Yamaguchi, An electromechanical Ising Hamiltonian, Sci. Adv. **2**, e1600236 (2016).

[15] M. Aspelmeyer, T. J. Kippenberg, and F. Marquardt, Cavity Optomechanics, Rev. Mod. Phys. **86**, 1391 (2014).

[16] M. Elyasi, Y. M. Blanter, and G. E. W. Bauer, Resources of nonlinear cavity magnonics for quantum information, Phys. Rev. B **101**, 054402 (2020).

[17] V. E. Demidov, O. Dzyapko, S. O. Demokritov, G. A. Melkov, and A. N. Slavin, Thermalization of a Parametrically Driven Magnon Gas Leading to Bose-Einstein Condensation, Phys. Rev. Lett. **99**, 037205 (2007).

[18] V. E. Demidov, O. Dzyapko, S. O. Demokritov, G. A. Melkov, and A. N. Slavin, Observation of Spontaneous Coherence in Bose-Einstein Condensate of Magnons, Phys. Rev. Lett. **100**, 047205 (2008).

[19] A. A. Serga, V. S. Tiberkevich, C. W. Sandweg, V. I. Vasyuchka, D. A. Bozhko, A. V. Chumak, T. Neumann, B. Obry, G. A. Melkov, A. N. Slavin, and B. Hillebrands, Bose-Einstein condensation in an ultra-hot gas of pumped magnons, Nat. Commun. **5**, 3452 (2013).

[20] D. A. Bozhko, A. A. Serga, P. Clausen, V. I. Vasyuchka, F. Heussner, G. A. Melkov, A. Pomyalov, V. S. Lvov, and B. Hillebrands, Supercurrent in a room-temperature Bose-Einstein magnon condensate, Nat. Phys. **12**, 1057 (2016).

[21] H. Suhl, The theory of ferromagnetic resonance at high signal powers, Phys. Chem. Solids **1**, 209 (1957).

[22] X. Y. Zhang and H. Suhl, Theory of auto-oscillations in high-power ferromagnetic resonance, Phys. Rev. B **38**, 4893 (1988).

[23] V. S. L'vov, *Wave Turbulence Under Parametric Excitation* (Springer-Verlag, Berlin, 1994).

[24] S. M. Rezende, Theory of coherence in Bose-Einstein condensation phenomena in a microwave-driven interacting magnon gas, Phys. Rev. B **79**, 174411 (2009).

[25] B. A. Kalinikos and A. N. Slavin, Theory of dipole-exchange spin wave spectrum for ferromagnetic films with mixed exchange boundary conditions, J. Phys. C: Solid State Phys. **19**, 7013 (1986).

[26] M. J. Hurben and C. E. Patton, Theory of magnetostatic waves for in-plane magnetized isotropic films, J. Magn. Magn. Mater. **139**, 263 (1995).

[27] D. D. Stancil and A. Prabhakar, *Spin Waves* (Springer, Berlin, 2009).

[28] P. Krivosik and C. E. Patton, Hamiltonian formulation of nonlinear spin-wave dynamics: Theory and applications, Phys. Rev. B **82**, 184428 (2010).

[29] S. M. Rezende, *Fundamentals of Magnonics* (Springer, Berlin, 2020).

[30] J. Barker and G. E. W. Bauer, Semiquantum thermodynamics of complex ferrimagnets, Phys. Rev. B **100**, 140401(R) (2019).

[31] M. Elyasi, E. Saitoh, and G. E. W. Bauer, Quantum correlations of the magnon parametron (unpublished).

[32] M. Elyasi and G. E. W. Bauer, Cryogenic spin Seebeck effect, Phys. Rev. B **103**, 054436 (2021).

[33] T. Hioki, H. Shimizu, T. Makiuchi, and E. Saitoh, State tomography for magnetization dynamics, Phys. Rev. B **104**, L100419 (2021).

[34] H. J. Carmichael, *Statistical Methods in Quantum Optics* (Springer, Berlin, 1999).

[35] D. F. Walls and G. J. Milburn, *Quantum Optics* (Springer, Berlin, 2008).

[36] P. H. Bryant, C. D. Jeffries, and K. Nakamura, Spin-wave dynamics in a ferrimagnetic sphere, Phys. Rev. A **38**, 4223 (1988).

[37] V. E. Zakharov, V. S. L'vov, and S. S. Starobinets, Spin-wave turbulence beyond the parametric excitation threshold, Sov. Phys.-Usp. **17**, 896 (1974).

[38] Introducing the phases $\phi_{\pm\vec{\mathcal{K}}}$ by $c_{\pm\vec{\mathcal{K}}} = |c_{\pm\vec{\mathcal{K}}}|e^{i\phi_{\pm\vec{\mathcal{K}}}}$, the four-magnon scatterings fix the sum $\phi_+ = \phi_{\vec{\mathcal{K}}} + \phi_{-\vec{\mathcal{K}}}$, but the difference $\phi_- = \phi_{\mathcal{K}} - \phi_{-\mathcal{K}}$ is not uniquely determined [37]. The magnetic disk has a large but finite radius that, strictly speaking, splits the continuum of states by $\Delta\nu \sim 2n\gamma D/r^2 \sim 10^4$ Hz, where $n = \lfloor 2r\mathcal{K} \rfloor \sim 4000$. Since $\Delta\nu \ll \xi_0$, the spectrum is still quasicontinuous, but the Kittel mode decays not into two propagating waves, but rather into a single standing wave mode. This can be formalized by combining the $\pm\vec{\mathcal{K}}$ pair of propagating waves as $c_{\pm\vec{\mathcal{K}}} = c_{\vec{\mathcal{K}}_s} e^{\mp iq/2}$ [36,37], where $q = \phi_-$ is a free phase that governs the position of the standing wave nodes and $\mathcal{K}_s$ is a state index. The reduction of a three-partite into a two-partite problem considerably simplifies the calculations in the quantum regime. Only the phase ϕ_+ affects the dynamics of the Kittel mode, which in the large dot limit is the same for both standing and propagating magnon modes, implying that the problem is bipartite from the outset.

[39] A. Chumak *et al.*, Roadmap on spin-wave computing, arXiv:2111.00365.

[40] P. Kinsler and P. D. Drummond, Quantum dynamics of the parametric oscillator, Phys. Rev. A **43**, 6194 (1991).

[41] W. F. Brown, Thermal fluctuations of a single-domain particle, Phys. Rev. **130**, 1677 (1963).

[42] A. A. Kovalev, L. X. Hayden, G. E. W. Bauer, and Y. Tserkovnyak, Macrospin Tunneling and Magnetopolaritons with Nanomechanical Interference, Phys. Rev. Lett. **106**, 147203 (2011).

[43] K. Hayakawa, S. Kanai, T. Funatsu, J. Igarashi, B. Jinnai, W. A. Borders, H. Ohno, and S. Fukami, Nanosecond Random Telegraph Noise in In-Plane Magnetic Tunnel Junctions, Phys. Rev. Lett. **126**, 117202 (2021).

[44] R. Landauer and J. A. Swanson, Frequency factors in the thermally activated process, Phys. Rev. **121**, 1668 (1961).